Materials & Design 215 (2022) 110492

Contents lists available at ScienceDirect

Materials & Design

journal homepage: www.elsevier.com/locate/matdes

Morphology changes in Fe-Cr porous alloys upon high-temperature oxidation quantified by X-ray tomographic microscopy

D. Koszelow [a], S. Molin [a], J. Karczewski [b], F. Marone [c], M. Makowska [d,*]

[a] Faculty of Electronics, Telecommunications and Informatics, Gdańsk University of Technology, Poland
[b] Faculty of Applied Physics and Mathematics, Gdańsk University of Technology, Poland
[c] Swiss Light Source, Paul Scherrer Institut, Villigen, Switzerland
[d] Laboratory for Nuclear Materials, Laboratory for Synchrotron Radiation and Femtochemistry, Paul Scherrer Institut, Villigen, Switzerland

HIGHLIGHTS

- A high-temperature oxidation at 850 °C (10 h, 30 h, 100 h) and 900 °C (10 h) of porous ferritic stainless steel Fe22Cr was performed and investigated by synchrotron tomographic microscopy.
- Tomographic analysis of corresponding regions in porous steel before and after corrosion.
- Distinguish metallic core, oxide scale, open and closed porosity phases.
- Quantification of microstructural changes such as specific surface area of steel, grain size distribution.
- 3D mapping of oxide scale thickness and pore size distribution.

GRAPHICAL ABSTRACT

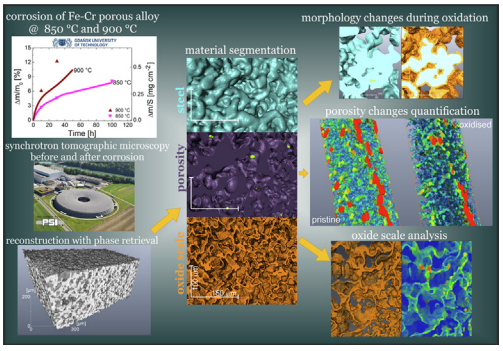

ARTICLE INFO

Article history:
Received 19 January 2022
Revised 16 February 2022
Accepted 24 February 2022
Available online 03 March 2022

Keywords:
Stainless steel
X-ray tomography
SEM
High-temperature corrosion

ABSTRACT

The effect of high-temperature oxidation at 850 °C (10 h, 30 h, 100 h) and 900 °C (10 h) on porous (~30 % porosity) ferritic stainless steel (Fe22Cr) has been investigated using synchrotron tomographic microscopy, which allowed for visualisation, separation and quantitative analysis of the metallic core, closed pores, open pores and oxide scale phase. The same regions within the samples were investigated before and after oxidation performed at different conditions. Quantitative analysis of the tomographic data provided information on changes upon oxidation of the relative volume of the different phases, the specific surface area (SSA) of the metallic core, the thickness of the oxide scale and pore size distribution. The results were discussed in the context of thermogravimetric analysis of the samples and supported by SEM imaging. It was observed that oxidation leads to an increase of the SSA of steel and the largest increase (~50 %) was obtained for the sample processed for 100 h at 850 °C. It is demonstrated the open porosity forms a network of connected channels within the sample and it dominates in the volume. In addition, the 3D imaging revealed breakaway oxidation areas for samples, for which this phenomenon remained undetected using 2D SEM analysis.

1. Introduction

Due to high corrosion resistance, high chromium content alloys are commonly used in certain types of nuclear reactors, turbines,

* Corresponding author.
E-mail address: malgorzata.makowska@psi.ch (M. Makowska).

https://doi.org/10.1016/j.matdes.2022.110492
0264-1275/

and engines [1-3]. The properties of dense chromia (Cr_2O_3) forming alloys have been thoroughly studied in recent decades and they are well described in the literature [4-6]. Selected ferritic steel alloys, such as Crofer 22 APU or Crofer 22H were proposed as interconnect materials in solid oxide fuel cell (SOFC) and solid oxide electrolysis cell (SOEC) stacks [7-9]. The main superiority of these alloys for application in solid oxide cells (SOC i.e. SOFC and SOEC) is high electrical conductivity of the chromia scale at operating conditions of SOC ($\sim$1 – 10 mS cm^{-1} at 600 – 800 °C) [10]. SiO_2 or Al_2O_3 forming alloys provide even higher corrosion resistance, but their much lower electrical conductivity disqualifies them for such applications in SOC. Typically, SOC interconnectors in commercial applications are produced from ceramic materials, however they are expensive and hard to manufacture in a specific shape. Thus, chromia forming alloys are considered a promising alternative for these components because of their electrical conductivity and ease of fabrication. Additionally, porous form of FeCr alloys can play a role of a support in metal-supported solid oxide cells (MS-SOC) because of decreasing the weight and cost of the whole device.

Porous steel alloys have been investigated intensively by many groups in the last years [11-13] because of their high application potential, for instance in gas membranes and sensor systems. The high amount of open porosity ensuring efficient gas transport is a prerequisite for the mentioned applications. On the other hand, open porosity results in orders of magnitude larger alloy-oxygen interface area, which may significantly accelerate the oxidation process. The oxide scale growth rate is a key factor for many potential applications of porous chromia forming alloys, since it leads to the limitation of the size of the pores or even closing the pore channels by filling them with chromia during oxidation. Deeper analysis of the oxidation mechanism of porous ferritic alloys, in particular the oxide thickness growth and corresponding morphology changes, closing porosity and the grain size distribution changes, is essential for enabling their usage in SOC and gas membranes as well as further broadening of their application field.

The mechanism of oxidation has been examined for dense ferritic alloys but the porous form of these alloys has not been evaluated in detail yet. Typically, the mechanism of oxidation is investigated based on mass gain measurements and SEM/EDX studies [5,14-17]. However, detailed information about oxide scale growth dynamics and grain distribution changes is still unknown. Up to now, there are only a few published works about the oxidation process of porous alloys [14,18-23].

Glasscock et al. [18] investigated the potential of using the porous Fe21Cr7Al1Mo0.5Y alloy as support for oxygen transport membranes. They showed that porosity $\geq$ 30 % with pore sizes much larger than the maximum oxide thickness of 3 μm is required to prevent pore-blockage by oxide scale growth and to ensure good gas transport throughout the lifetime of the device. The changes of the alloy porosity were determined using BET adsorption, mercury porosimetry, and image analysis of SEM micrographs. These methods allow for calculating the percentage of pore volume and estimation of the pore size distribution but information about changes of SSA and oxides scale morphology after oxidation is still missing.

The most common tool used for determining microstructural changes of the alloy due to oxidation is scanning electron microscopy (SEM)[14], which, however, allows only for analysing randomly selected cross-sections of the sample in 2D. The oxide scale thickness cannot be properly evaluated from 2D images, as the observed thickness depends on the orientation of the scale layer with respect to the cross-section plane. Moreover, this value can be inaccurate because of the irregular growth of the oxide scale [24]. Therefore, analysis of the scale thickness should be performed taking into account the 3 - dimensional geometry of the material and based on the imaging of a representative volume of samples, and not only a cross-section.

X-ray tomographic microscopy (also called micro computed tomography, μCT) is a non-destructive method, which provides insight into the 3-dimentional morphology of different phases in a material and enables their relative volumetric quantification, if these phases are characterized by sufficient contrast [25]. This advanced method was used for the observation of microstructure changes, phase composition changes, and damage mechanisms of different alloys by several research groups [26-37]. Kapat et al. have investigated the influence of porosity and pore size distribution in a Ti6Al4V foam on its physicomechanical properties for medical implant applications [26]. The porosity was determined via 2D SEM image analysis, water displacement method and from synchrotron tomographic microscopy. The decrease of porosity was linked to the reduction of pore connectivity. Mokhtari et al. [31] analysed FeCr alloys with a 30 – 70 % range of porosity created by a dealloying process. The authors used tomographic microscopy for calculation of the SSA and average pore size. Le et al [30] investigated the effect of porosity on the fatigue behaviour of AlSi7Mg0.3 alloys obtained by the lost foam casting process. They showed that stress concentrations at the pores are increased and lead to local plasticity. Additionally, simulations of the influence of pore shape on fatigue strength were performed and indicated the real casting pores (more irregular) provide more significant sensitivity on fatigue strength compared with spherical pores. Thus, the examination of the real structure of porosity is essential for predicting the properties (and lifetime) of the alloys. Synchrotron tomography was also applied for studies of the porosity evolution in freeze-cast iron foams [38,39] using setup providing voxel size of 2.45 μm. In several works, laboratory μCT with 2.5 μm voxel size was performed to provide data on porosity, necessary to be used in modelling of mechanical properties of porous alloys [40,41]. In our recent work, we have demonstrated that synchrotron tomographic microscopy allows for the separation and quantification of porosity, metallic core, and oxide scale phases in porous ferritic steel [24].

X-ray tomographic microscopy provides insight into the 3-dimensional morphology, while SEM is limited to 2D images. Electron microscopy allows however resolving features of dimensions beyond the spatial resolution of the μCT technique, meaning that SEM images allow for recognising more details in the microstructure. For instance, nitride precipitate that can appear during oxidation of the high chromium ferritic alloys [6,42,43] with a size from submicron to a few microns are at the edge of the capabilities of μCT. Thus, it might be possible to detect them, but not to analyse their morphology. Achieving higher resolution with μCT is possible at the expense of a significant decrease of the field of view, nevertheless, the resolution achievable with SEM cannot be reached by μCT. In this work, it was important to investigate volume large enough to obtain representative statistics of the measured quantities keeping a possibly high spatial resolution of images. Therefore, we use both electron microscopy and synchrotron tomographic microscopy as complementary methods, as such approach allows for complex 3-dimensional analysis of the sample in a broad size scale range, providing a full picture of morphology changes in porous steel upon oxidation.

In this work, results of detailed studies of the 3-dementional morphology the porous Fe22Cr alloy oxidised in air at 850 °C and 900 °C are presented. Specimens were investigated with SEM and synchrotron tomographic microscopy before and after ex-situ oxidation. For tomographic measurements before and after oxidation, exactly the same area of each sample was localised, analysed and the morphology before and after the process was compared. The results allowed for evaluation of changes upon oxidation of the SSA of the metallic core, oxide thickness and average grain size

of the alloy for different oxidation conditions (time, temperature). Moreover, breakaway oxidation centres were identified. To the best of our knowledge, this is the first work addressing the changes in microstructure, grains size, and oxide thickness of chromia forming porous alloys by three-dimensional analysis.

2. Experimental

2.1. Sample preparation

A porous alloy sheet ~ 100 × 100 mm^2 with a thickness of 0.35 mm was obtained from Höganäs AB (experimental alloy MW2, Höganäs, Sweden). It was prepared by a tape-casting process from a steel powder slurry, followed by drying, debinding, and sintering in a reducing atmosphere (1250 °C, 30 min, H_2). The porosity of the alloy determined by the producer is 30 %. Chemical composition of the alloy is presented in Table 1. Three series of samples were prepared from the 0.35 mm thick sheet, which was cut into smaller pieces of different sizes depending on the performed experiment. In the first series, for the thermogravimetric analysis, ~3 × 3 × 0.35 mm^3 pieces of the alloy were prepared. The second series was prepared for the ex-situ oxidation measurements, with dimensions of ~ 10 × 10 × 0.35 mm^3, and for X-ray tomography, the third series consisted of elongated samples (~6 × 1 × 0.35 m m^3). Before use, samples were cleaned in an ultrasonic bath in ethanol (99.9 %) followed by acetone (99.9 %).

2.2. Thermogravimetric analysis

The thermogravimetric analysis during oxidation of the alloy was performed using a Netzsch TG 209 F3 Tarsus thermobalance. The heating and cooling rates were 3 °C min^{-1}. The experiment was carried out in air atmosphere with a flow rate of 50 ml min^{-1}. Samples were exposed to a corrosive environment for 100 h at 850 °C and for ~ 40 h at 900 °C (due to instabilities of the thermobalance for long measurements at high temperature). The results were plotted as the relative mass change of the sample and mass gain per surface area of the sample (determined from the tomography measurements) over time.

2.3. Scanning electron microscopy

The second series of samples was oxidised ex-situ for 10 h, 30 h, and 100 h at 850 °C and 900 °C for evaluation of the alloy morphology changes. SEM imaging was performed using a Phenom XL electron microscope (Thermo Fisher Scientific, Netherlands) on polished cross-sections of the samples. All SEM images were recorded using backscatter electron detector (BSE). The microscope is equipped with an EDX detector (Thermo Fisher Scientific, 25 mm^2 Silicon Drift Detector), which was used for elemental analysis of the steel (EDX analyses performed at acceleration voltage of 15 kV).

2.4. Synchrotron tomographic microscopy

Samples for the tomography investigation were oxidised under the same conditions, as the samples for the SEM studies. X-ray tomographic microscopy characterization of samples was performed at the TOMCAT beamline of the Swiss Light Source (SLS) at the Paul Scherrer Institute, Villigen, Switzerland. A parallel X-ray beam with an energy of 40 keV was used. The detector setup was composed of a scintillator converting X-rays into visible light, an objective lens and a sCMOS camera with settings resulting in a field of view (FOV) of approximately 0.8 mm × 0.8 mm and an image pixel size of 0.325 μm. A total of 1001 projections over 180° were recorded, each with 1600 ms exposure, resulting in scans lasting about 26 min. Each sample was investigated using exactly the same setup before and after exposure to corrosive conditions. During measurements after oxidation, the same region of the sample, which was scanned before oxidation, was localised and measured with identical parameters.

The reconstruction of the acquired tomograms was conducted using the in-house developed pipeline available at the beamline that provides complete tomographic volumes immediately after data acquisition, allowing for quick adjustment of measurement and reconstruction algorithm parameters. The acquired projections were tomographically reconstructed after dark- and flat-field correction and phase retrieval with the Paganin algorithm [44]. Phase retrieval was helpful in increasing the signal-to-noise and contrast-to-noise ratios. The achieved contrast in the images reconstructed with this approach allowed for a relatively straightforward material segmentation based only on intensity thresholding, which was performed using the commercial software Avizo 9.4. The intensity ranges that were assigned to steel, porosity and oxide scale, were selected based on the histogram minima defined for one of the samples with a high oxidation degree (here referred to as CT900.10). Then, exactly the same intensity ranges were applied to all the analysed samples for segmentation of the particular phases. The reconstruction provided 16-bit images with a dynamic range from 0 to 65535, and it was calculated, that an increase by 1% of the threshold value used for the steel phase, would result in higher fraction of this phase by 0.5%. Although the absolute values of calculated material fractions depend on the selected intensity thresholds, applying the same intensity ranges for all the samples allows for reasonable comparison of the oxidation-induced changes. It was observed that the oxide scale of thickness about 1 μm was possible to detect in the reconstructed volumes, thus, 1 μm was further considered as a spatial resolution of the analysed images.

Avizo software was also used to evaluate the oxide scale thickness distribution and to perform alloy grain separation for evaluation of the grain size distribution. Moreover, a comprehensive porosity analysis was performed, which allowed for estimating changes upon oxidation of the average pore channel cross-section as well as changes of the amount of open, closed and total porosity. Direct comparison and observation of microstructural alterations from the non-oxidised to oxidised state of the samples was possible, since exactly the same region in the measured volumes in both states was localised and analysed.

The role of porosity for applications of the allows as SOFC/SOEC interconnects or gas membranes is connected to the efficiency of gas transport. Thus, in this work, for the evaluation of the porosity changes upon oxidation, the pores are considered as a network of channels. The distribution of the pore channel thicknesses was evaluated using an algorithm that computes the local thickness of a selected material for each voxel in the binary volume. In this

Table 1
Chemical composition of the alloy (provided by the producer).

		Analyzed chemical composition, %										
Target composition	Fe	Cr	Ni	Mo	Mn	Cu	Si	Nb	C	O	N	S
Fe22Cr	Bal.	22.0	0.03	0.01	0.23	0.02	0.08	0.02	0.04	0.58	0.07	0.01

particular case, the binary volume consisted of pore pixels labelled with "1" and other pixels (for any kind of material) labelled with "0" are assigned to all the other voxels. The local thickness is defined as the diameter of the largest possible ball containing this voxel and fully inscribed within the analysed material (in this case pores). This commonly used approach has been described in detail in [45] and is implemented in the Avizo software in the "Thickness Map" module. The same approach and algorithm were used for determining the oxide scale thickness.

3. Results and discussion

3.1. Thermogravimetric analysis

Relative mass changes of the samples during exposure to air at temperatures of 850 °C and 900 °C are presented in Fig. 1. The thermogravimetric data were compared with separate ex-situ mass measurements. For samples oxidised at 850 °C, ex-situ (pink data points in Fig. 1) and isothermal mass gains (pink solid line) are comparable, but for alloys oxidised at 900 °C, significantly different values were obtained. However, in the case of the ex-situ oxidation, the samples spent a longer time at high temperatures due to the heating and cooling process. For such a high temperature as 900 °C, it can cause higher values of ex-situ measured mass gain but the oxidation rate is considerably slower at lower temperatures so, this effect is negligible for samples oxidised at 850 °C. A previous investigation [24] has shown that the oxidation process of porous Fe22Cr alloy follows a parabolic rate law thus, its kinetics is limited by diffusion of Cr^{3+} cations. The threshold level of mass gain for breakaway oxidation appearance was established as about 6 wt%.

3.2. SEM analysis of samples before and after oxidation

EDX analysis on polished cross-sections was used to evaluate the alloy's chemical composition. The final results were 21.3 wt% Cr and 0.26 wt% Mn, with iron as a balance. Taking into consideration the relatively high inaccuracy of the EDX method, the chemical composition was in agreement with the producer data. The morphology of the surface and polished cross-section of the alloy is presented in Fig. 2. The particles are well connected and necks between the grains are well visible (Fig. 2D). Also from cross-section images, the interfaces between grains are noticeable (Fig. 2B).

Fig. 3 shows the SEM images of oxidised samples. The sample oxidised at 850 °C for 10 h is presented in the first column (Fig. 3 A, E, I). Images taken at higher magnification revealed the presence of a thin layer of an oxide scale varying in thickness in the range of 1–2 μm. The oxide scale observed for a sample oxidised at 850 °C for 30 h (Fig. 3 B, F, J) appears locally thicker (1–4 μm) than it is for a sample that has been oxidised for 10 h. Further oxidisation of the alloy up to 100 h (at 850 °C) leads to breakaway oxidation (Fig. 3 C) which, in this case, appeared at the surface of the sample. The sample was penetrated up to 150 μm by the breakaway oxidation area. Even at lower magnifications, the oxide scale around the grains is visible on the whole cross-section. The oxide thickness observed in these images (Fig. 3C, G and K) does not significantly differ from the sample oxidised at 850 °C for 30 h (Fig. 3 B, F, J) and can be estimated to 1 – 5 μm. For the alloy oxidised at 900 °C for 10 h (Fig. 3 D, H, L) breakaway oxidation was not observed in the prepared cross-section and the oxide thickness was approximately 2–5 μm, which is comparable with both, the sample oxidised at 850 °C for 100 h, and the sample oxidised at 850 °C for 30 h. However, the tomographic microscopy experiment has revealed that the breakaway oxidation region occurred also for the sample oxidised at 850 °C for 30 h (CT850.30) and for the sample oxidised at 900 °C for 10 h (CT900.10) but this aspect will be elaborated in the next section. In our previous work, a change in the slope of the thermogravimetric curve after 10 h of oxidation at 900 °C was observed. It corresponds to 6% mass gain which was determined as the breakaway oxidation appearance threshold value for Fe22Cr alloy [24]. This confirms that analysis of SEM images is not sufficient to determine changes in alloy morphology and 3-dimensional analysis is necessary for accurate breakaway oxidation region detection.

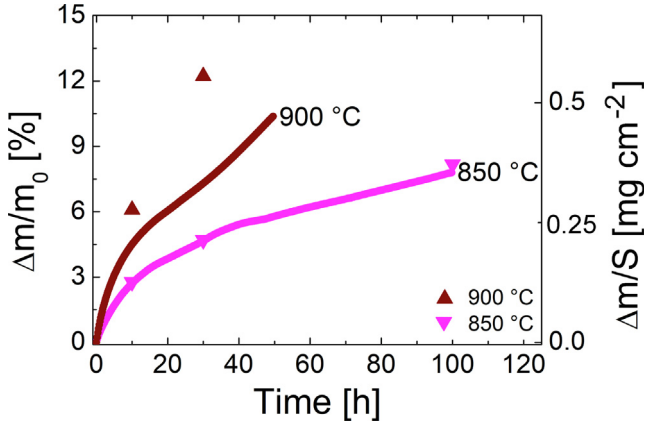

Fig. 1. Isothermal (solid line) and ex-situ (markers) mass gain of samples oxidised at 850 °C and 900 °C.

3.3. Synchrotron tomographic microscopy

3.3.1. Oxide scale thickness and morphology

Although SEM imaging allows for estimation of the scale thickness, as discussed in the introduction, its evaluation from 2D cross-sections can be misleading. Moreover, there might be some variations in the whole volume. For instance, the breakaway oxidation centres appear as large, irregular features in locations remote from each other. Therefore, their size cannot be evaluated from the 2D cross-section of a sample, as the result strongly depends on the location of the cross section. Moreover, the breakaway oxidation centres can be easily overlooked if the cross-section is prepared in a wrong location. Thus, for a detailed analysis of the complex morphology of the alloy, synchrotron tomographic microscopy was performed. Detailed information about mass changes for the samples used in the tomography experiment was gathered in Table 2. The applied sample name relates to the series of the sample after tomography measurement in order to distinguish results from tomography from the other techniques.

Fig. 4 presents a visualisation of sample CT850.100 before (Fig. 4 A) and after (Fig. 4 B) oxidation obtained by volume rendering of the reconstructed data with reconstructed slices (Fig. 4 C and D) corresponding to the clipping planes visible in the 3D images Fig. 4 A and B (the front planes). The necks between the grains are clearly visible and in the case of the oxidised samples, it is apparent that the contrast between different phases allows to distinguish the oxide phase from the metallic core. Consequently, material segmentation was performed for each sample, and its material statistics (summarized in Table 3) evaluated.

Oxide growth, caused by diffusion of either cations or anions, is a temperature activated process. Our previous research [24] has shown, that indeed, temperature plays a key role in oxidation kinetics of porous alloys.. Thus, this study is focused on the comparison of the oxidation process for samples oxidised at different temperatures, but with the same holding time. Fig. 5 and Fig. 6 present results of material segmentation before and after exposure for

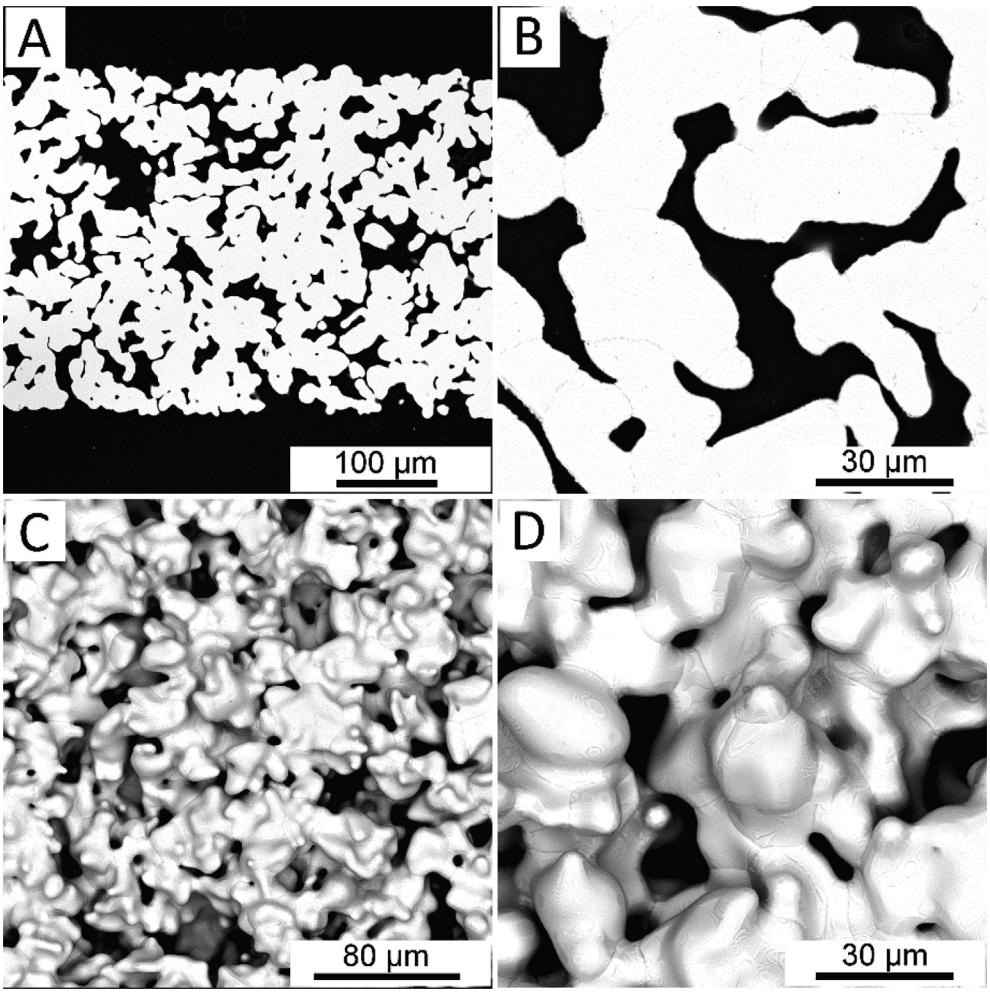

Fig. 2. SEM images of A, B) cross-section; C, D) surface of as-received MW2 alloy.

CT850.10 and CT900.10 samples, respectively. For both samples, the same region before (Fig. 5 A, Fig. 6 A) and after (Fig. 5 B, Fig. 6 B) oxidation is presented. As seen in both Fig. 5 and Fig. 6, the oxide scale has grown on the surface of the alloy's grains. In the case of sample CT850.10 (Fig. 5), the oxide scale is relatively smooth and covers tightly the grains surface. In the SEM images there is a small oxide roughness visible (Fig. 3I) for this sample, but it cannot be resolved in tomographic images. The roughness of the oxide scale in CT900.10, appears significantly larger (Fig. 6) as compared to CT850.10 (Fig. 5). Additionally, some porosity within the oxide scale is present, which was also observed in SEM images of a sample oxidised under the same conditions (Fig. 3H).

Based on the obtained segmentation results, the oxide scale thickness was evaluated using the "Thickness Map" module for each voxel of the oxide phase, which allowed for visualisation of the oxide thickness distribution. Examples of such visualisation are illustrated in Fig. 7 A, C for sample CT850.30 and in Fig. 7 D for sample CT900.10, which show 3-dimensional maps of the oxide thickness. Fig. 7 B illustrates volume rendering of the oxide phase in the corresponding region of sample CT850.30, based on which the thickness map in Fig. 7 A was evaluated. The colour scale assigned to voxels in Fig. 7A reflects the thickness of the oxide layer evaluated for the corresponding voxels. As seen in Fig. 7A, the breakaway oxidation area could be clearly identified for the CT850.30 sample. Taking into consideration the whole investigated volume of this sample, even more regions with breakaway oxidation were found, supporting the higher mass gain measured for the CT850.30 sample compared to sample CT900.10 (Table 2). In contrast, the average thickness of the oxide scale is larger for CT900.10 (Table 4) because as seen in Fig. 7 C and Fig. 7 D, the colour scale for the CT900.10 sample is shifted towards the red colour in comparison to the sample CT850.30 colour scale for the whole presented volume. For a deeper understanding of the places of breakaway oxidation origin, in situ experiments are necessary. Based on such thickness maps generated for each of the investigated samples, the corresponding histograms were evaluated, which are shown in Fig. 8.

In the histograms in Fig. 8, there is a clear maximum visible for each investigated sample, except for CT850.10, which had the lowest oxidation degree. The lack of a peak in the CT850.10 oxide thickness histogram is related to the spatial resolution, which in this case is about 1 μm. Objects beyond this resolution, for instance oxide layers thinner than 1 μm, cannot be assessed based on these data. Thus, the sample CT850.10 is at the edge of the capabilities of tomographic microscopy performed with parameters selected for this work and therefore, this method could not be applied to samples with a lower degree of oxidation than CT850.10. Based on the oxide thickness histograms, the mean oxide thickness values were calculated and summarized in Table 4. For the CT850.10 sample it was 1.12 μm, for the CT850.30 sample oxidised the oxide scale thickness was 2.11 μm and it increased to 2.45 μm for samples CT850.100 and CT900.10. These values are lower than in the case of SEM images analysis of the oxide scale thickness. However,

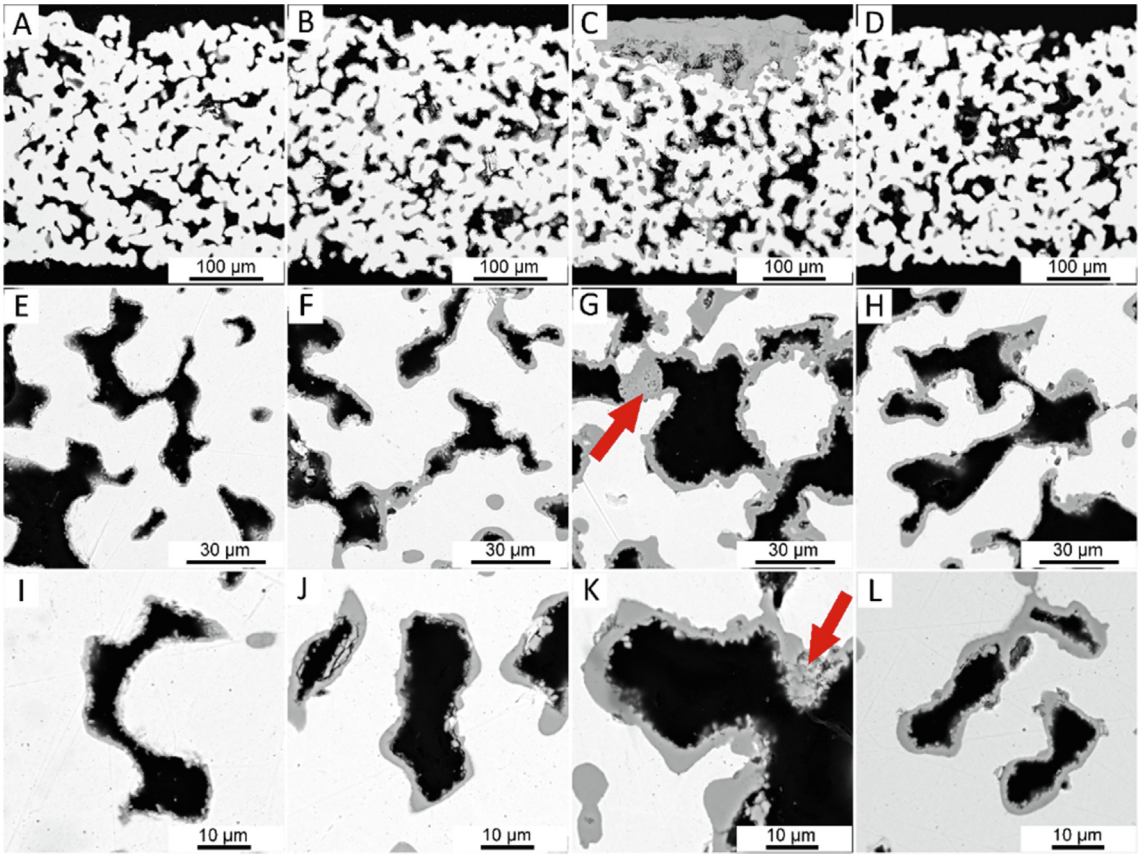

Fig. 3. SEM cross-section images of the alloy oxidised A, E, I) for 10 h at 850 °C; B, F, J) for 30 h at 850 °C; C, G, K) for 100 h at 850 °C; D, H, L) for 10 h at 900 °C. The red arrows indicate the porosity and roughness of the oxide scale. (For interpretation of the references to colour in this figure legend, the reader is referred to the web version of this article.)

Table 2
List of samples with mass changes.

Sample name	Oxidation conditions	Initial weight [mg]	Final weight [mg]	$\Delta m/m_0$ [%]
CT850.10	850 °C, 10 h	18.13	18.61	2,65
CT850.30	850 °C, 30 h	7.35	7.77	5.71
CT850.100	850 °C, 100 h	13.75	14.90	8.36
CT900.10	900 °C, 10 h	12.84	13.53	5.37

SEM images show only a specified slice, which does not represent the whole sample volume, so the results of the tomography-based calculations are more comprehensive.

Material segmentation allows for calculation of the amount of different phases (alloy – oxide - pore), which is directly linked to the oxidation degree. In sample CT850.10, the oxide scale occupies 18.8 % of the sample‘s volume (volume occupied by a material, excluding porosity), which is calculated from the material segmentation results (Table 3), as a fraction of the volume of the oxide divided by the sum of alloy and oxide scale‘ volumes. The volume of the of the oxide scale contribution calculated for this sample from the measured mass gain (Table 2), is 11.6 %. Such difference is caused by several factors. Small porosity and roughness of the oxide scale visible in SEM images (examples are marked with the arrows in Fig. 3G and K) cannot be resolved in the tomograms. Therefore, the volume assigned to the oxide scale evaluated from the tomographic data, includes also these features and thus, it is significantly larger than the value obtained from the mass gain measurements that consider only fully dense material. Possible other reason might be a changing volume of the alloy phase, based on a decreasing diameter of alloy particles, altering oxide growth from a typical outward diffusion driven to a complex one, where formation of internal porosity/voids can be expected. In other words, porosity and roughness beyond the resolution were labelled as the oxide material and thus, the oxide phase assigned via material segmentation has a lower density than theoretical Cr_2O_3 density.

In case of sample CT900.10, the fraction of the oxide phase based on material segmentation results (Table 3) was 34.9 % of the sample‘s volume, again assuming that the total sample volume is a sum of oxide scale and alloy contributions (Table 3). Based on mass gain data of the same sample (Table 2), the determined oxide scale fraction is 22.2 %, which is a significantly lower value as compared to tomography-based calculations. The roughness and porosity of the oxide scale in CT900.10, which partially are not resolvable in tomography, as well as the microstructural changes, are significantly larger (Fig. 6) compared with CT850.10 (Fig. 5), so the difference of the oxide scale contribution calculated based on tomographic microscopy and mass gain data is even more significant in case of CT900.10. As mentioned above, these calculations of phase fraction do not take into account the porosity and roughness of the oxide scale, which is beyond the tomographic

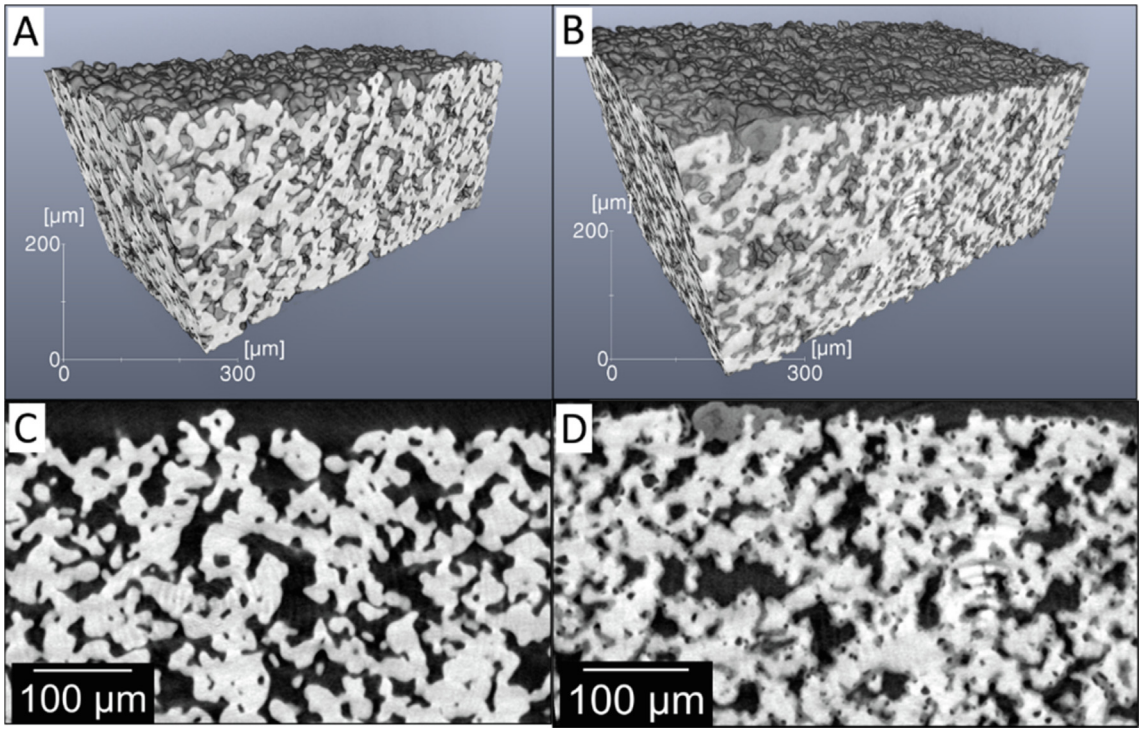

Fig. 4. Volume rendering of the reconstructed tomographic volume of sample CT850.100 a) before and b) after oxidation with reconstructed slices corresponding to the clipping planes (front planes) in the 3D images.

Table 3
Material statistics before and after oxidation (vol %).

Sample	Oxidation conditions	Steel		Oxide		Open pores		Closed pores		Oxide / (Oxide + Steel)
		Before	After	Before	After	Before	After	Before	After	After
CT850.10	850 °C, 10 h	67.85	62.46	–	14.42	32.04	22.97	0.10	0.14	18.76
CT850.30	850 °C, 30 h	67.57	57.40	–	20.50	32.35	22.00	0.07	0.10	26.32
CT850.100	850 °C, 100 h	67.40	52.70	–	26.80	32.51	20.40	0.09	0.10	33.71
CT900.10	900 °C, 10 h	61.41	46.50	–	24.90	38.52	28.50	0.07	0.10	34.87

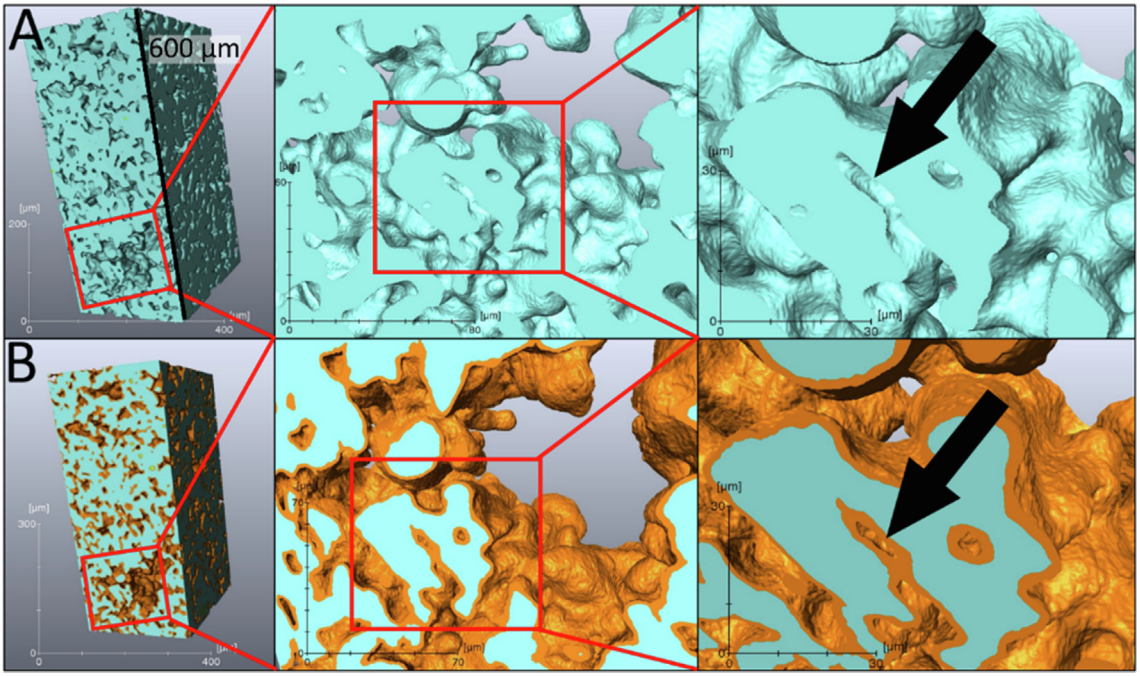

Fig. 5. Visualisation of the metallic core (turquoise) and oxide scale (orange) based on volume rendering of the results of material segmentation for sample CT850.10 A) before oxidation, B) after oxidation at 850 °C for 10 h. Black arrows show exemplary regions where pore channels are blocked by the oxidation process. (For interpretation of the references to colour in this figure legend, the reader is referred to the web version of this article.)

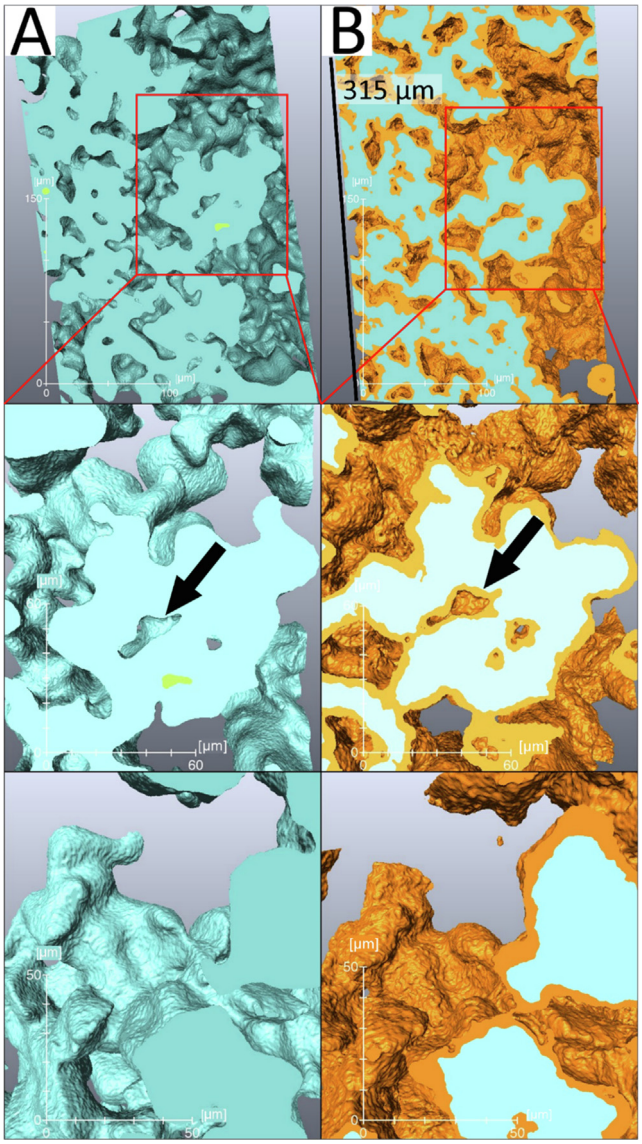

Fig. 6. Visualisation of the metallic core (turquoise), the oxide scale (orange) and the closed porosity (green) based on volume rendering of the results of material segmentation for sample CT900.10 A) before oxidation, B) after oxidation at 900 °C for 10 h. Black arrows show exemplary regions where pore channels are blocked by the oxidation process. (For interpretation of the references to colour in this figure legend, the reader is referred to the web version of this article.)

microscopy resolution (around 1 μm^3), though still visible in SEM images.

Detailed statistics of phase composition for each sample were gathered in Table 3. For each of the investigated samples, the consumption of the steel phase is clearly visible. The longer the oxidation time, the more advanced the transition of the alloy into the oxide scale is observed like in the case of CT850.100 and CT900.10. The contribution of the oxide scale for the CT900.10 sample is similar to the CT850.100 sample, which demonstrates the strong temperature effect on the oxide scale growth.

Higher oxidation degrees lead to the breakaway oxidation observed as large oxide agglomerates in certain locations. Understanding their formation process is crucial for the usage of the alloy because it determines the lifetime and possible applications of the alloy. In Fig. 7, presenting a map of the oxide scale thickness with corresponding oxide scale morphology of the same region, the breakaway oxidation centre is clearly observed as the red colour area. Similar features were detected also in the measured volumes of CT850.100 and CT900.10 samples (not shown here). The average oxide scale thickness for the CT850.30 sample is 2.11 µm (Table 4) but locally it reaches significantly higher values in the breakaway oxidation region. According to the SEM analysis, the breakaway region appears only for the sample oxidised at 850 °C for 100 h but the tomographic experiments revealed that it has occurred also for the CT850.30 and CT900.10, demonstrating the necessity of the 3D analysis for detailed oxidation process research. The results of tomography studies presented here, indicate that the previously established threshold for breakaway oxidation appearance of ~ 6 wt% mass gain was slightly overestimated, since breakaway oxidation also occurs for lower mass gain values, as in case of samples CT850.30 (5.71 wt%) and CT900.10 (5.37 wt%).

3.3.2. Specific surface area and particle size

Material segmentation of the reconstructed volumes allows for generating a surface of each selected material, and consequently to evaluate its SSA, as a ratio of the surface area and weight. The SSA of the non-oxidised alloy was 0.020 m^2g^{-1} and it was observed that it changes after the oxidation process depending on the time of oxidation and on the temperature. The obtained values (Table 4) show a 10 % growth of SSA after 10 h of oxidation at 850 °C (CT850.10), while after 100 h at the same temperature (CT850.100), SSA grew by>50%. A similar increase (~50 %) was observed for the CT900.10 sample. During oxidation, the oxide scale growth is irregular (as showed in Fig. 6), so the surface of the remaining alloy becomes more irregular as well, which explains the increase in its surface. It should be noted that due to the resolution limitation, in case of the more oxidized samples SSA might underestimated, however in the SEM images we observe that the fine roughness and porosity, which is not resolved in tomography is significant rather for the oxide scale, and less significant for the steel, for which SSA is evaluated.

Additionally, the total weight of the alloy fraction becomes smaller, which was also evaluated based on the obtained material statistics. Thus, the SSA of the alloy increases during the oxidation process. This results in an increased oxygen-alloy contact area, which in turn, facilitates further oxidation. On the other hand, oxide scale growth provides a diffusion barrier for chromium cations, which slows down the oxidation process. In the case of the investigated samples, this effect seems to counterbalance the effect of SSA growth.

Another important factor in the oxidation process is the grain size distribution of the porous alloys, as it is strongly related to the SSA. Moreover, oxidation processes of porous Fe22Cr alloy are determined by the diffusion of Cr^{3+} cations from the bulk to the surface, so for smaller particles, the diffusion path is shorter, which in turn accelerates the oxide scale growth. Tomographic microscopy is a well-suited tool for analysis of the particle size in porous alloys. For this purpose, particle separation was performed for the binary volume of the metallic core separated from other phases, which allowed for evaluation of statistics of steel particle size. Table 4 provides detailed information on particle size for each investigated sample. Average particle size before oxidation was very similar for each sample and it decreased during the oxidation. Surprisingly, the largest change was observed not for the sample CT850.100, which reached highest mass gain, but for the sample CT900.10, which was oxidised at highest temperature. The measured particle size was not related to the oxide morphology, so the observed effect may be linked to the more advanced breakaway oxidation in sample CT850.100. However, due to the change of particles morphologies, it is often not possible to justify if the particle separation was performed correctly for samples after oxidation. Therefore, such analysis should be performed via in-situ experiments. Further details, how the particle size distribution

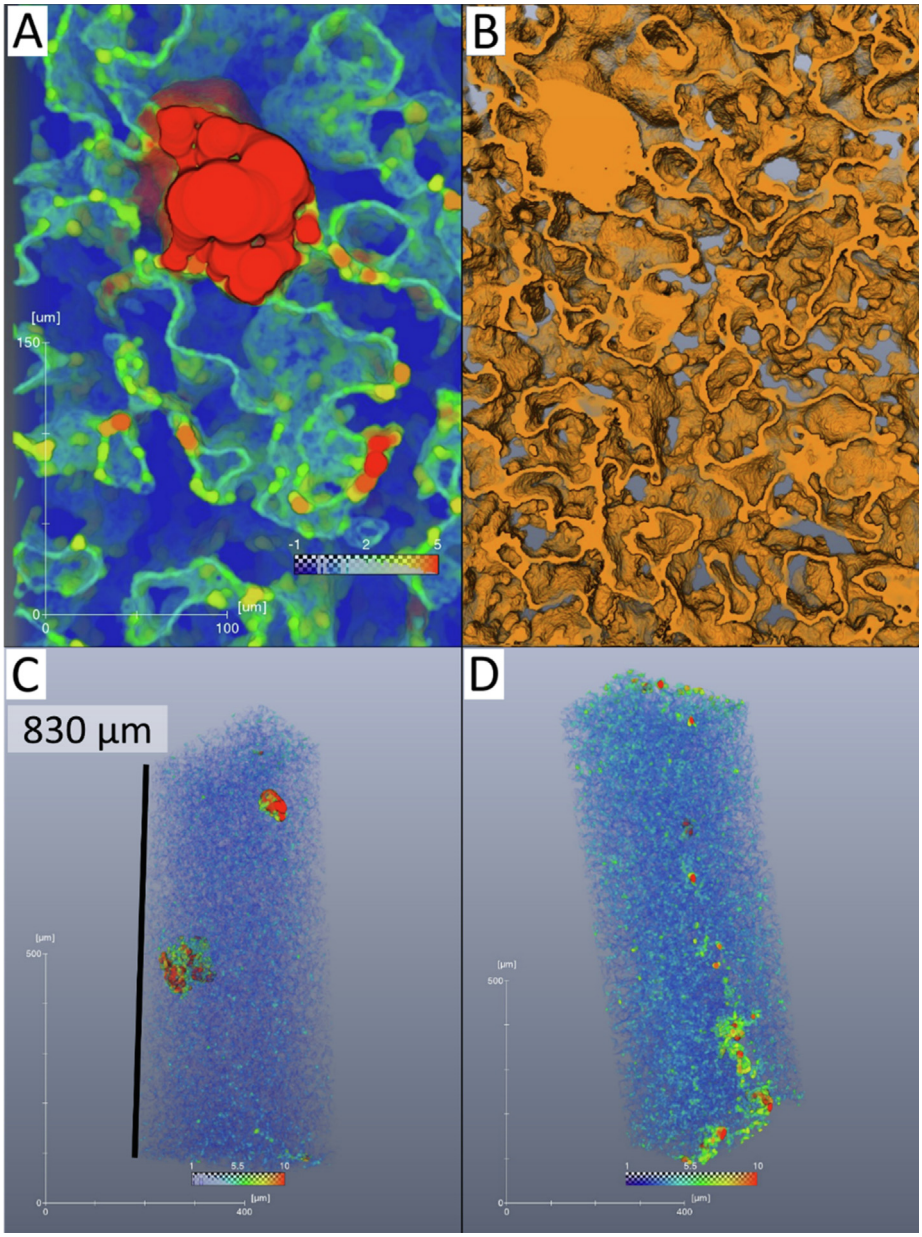

Fig. 7. A, C) Oxide scale thickness map for the CT850.30 sample with B) corresponding morphology of the same sample region and comparison with D) the oxide scale thickness map for the CT900.10 sample.

analysis was performed are presented in the supplementary material.

3.3.3. Effect of oxidation on porosity

Analysis of the tomographic measurements clearly demonstrate that the open porosity dominates for the investigated alloy and creates a system of connected channels, which is crucial for applications requiring efficient gas transport through the material, as it is required for instance in membrane systems. Oxidation leads to the growth of the oxide scale resulting in formation of closed porosity and blocking of some pore channels, as it is visible for instance in Figs. 5 and 6 in the locations marked by black arrows. However, the obtained material statistics (Table 3) shows that even after oxidation of the sample CT850.100, for which the most advanced oxidation degree was reached, the initial character of porosity was maintained, since the closed porosity was only ~ 0. 1 vol% of whole sample volume.

More importantly, during oxidation the overall porosity volume fraction and the size of the pore channels decrease because of the oxide scale growth. The porosity of the raw alloy calculated from the tomographic data varied between 32.0% and 32.5% for samples CT850.10, CT850.30 and CT850.100, which is in agreement with a value obtained with Archimedes method of 31% (±2%). The sample CT900.10 had a significantly larger initial porosity of 38.2%. After oxidation, the porosity of samples has decreased to ~ 23%, 22%, 20.4% and 28.5% (Table 3) for samples CT850.10, CT850.30, CT850.100 and CT900.10, respectively. These results, especially for sample CT900.10, show the importance of comparing the porosity before and after oxidation for the same volume, as the initial values may vary.

The size of the pore channels was evaluated as the "pore thickness", which was calculated for each voxel using the same Thickness Map module, as for the oxide thickness evaluation. For the calculation of the average pore thickness, pores with a diameter

Table 4
Evaluation of morphology changes.

Sample name	Specific surface area (SSA) [m^2/g]		Average particle size [μm] (>6 μm) **(average gauss fit)**		Average pore thickness > 1 μm) **(lognormal fit > 1 μm)**		Oxide thickness	
	Before	After	Before	After	Before	After	Before	After
CT850.10	0.020	0.022	32.5	31.5	13.6	12.6	–	1.12
			32.7	**32.0**	**14.0**	**12.4**		
CT850.30	0.020	0.027	31.3	27.6	13.0	10.1	–	2.11
			30.4	**27.8**	**15.0**	**10.8**		
CT850.100	0.020	0.031	30.5	26.7	12.5	10.3	–	2.45
			30.2	**27.0**	**14.5**	**11.0**		
CT900.10	0.020	0.030	31.0	26.7	16.5	14.8	–	2.45
			31.4	**27.1**	**17.9**	**15.4**		

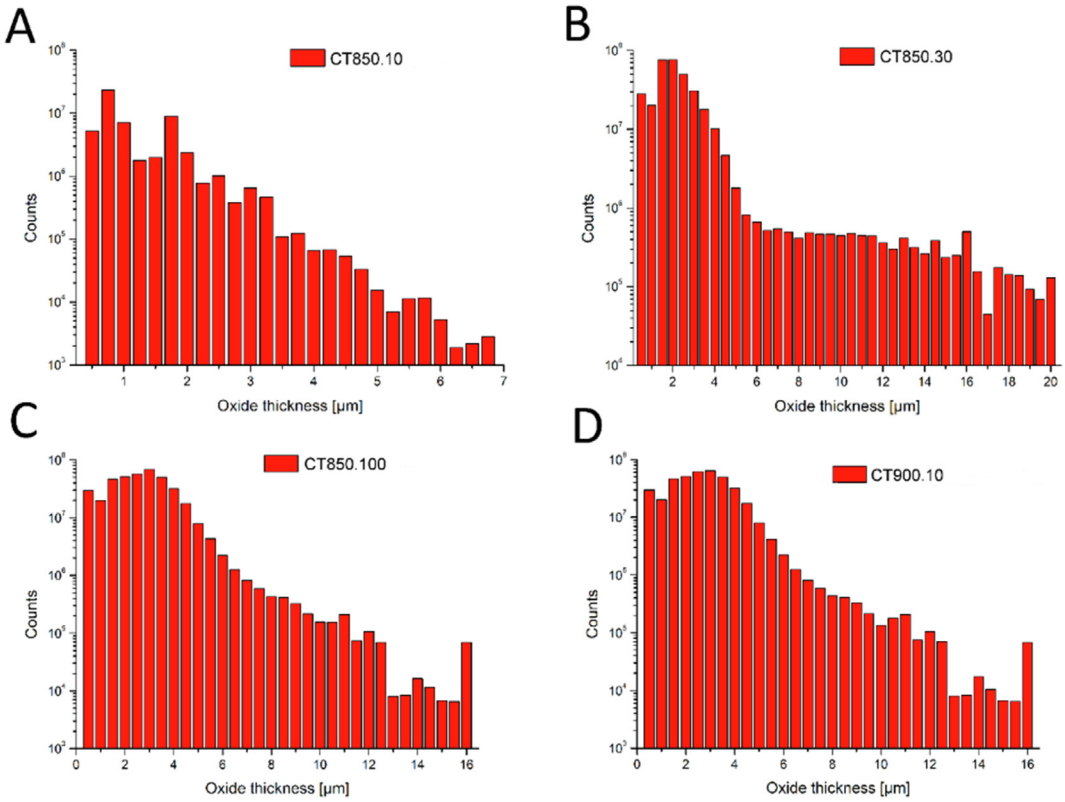

Fig. 8. Oxide scale thickness distribution for A) CT850.10, B) CT850.30, C) CT850.100, D) CT900.10.

below 1 μm were excluded from the statistics. As mentioned in the previous sections, there are cracks within the oxide scale, which are visible in SEM images (Fig. 3 K). In the case of tomography measurements, they are not detected but they appear as a small change in the grey scale. Moreover, such small objects do not significantly change the total porosity, as their fraction in the whole porosity is negligible.

The morphology and size distribution of porosity of samples CT850.10 and CT900.10 is illustrated in the 3-dimensional maps in Figs. 9 and 10, respectively. The colour scale corresponds to the pore size value (blue is assigned to the smallest pores and red to the biggest ones). Fig. 9A and 10A represent the porosity thickness before oxidation and Fig. 9B and 10B after oxidation for CT850.10 and CT900.10, respectively. In both cases, the colour scales are shifted towards the blue colour after oxidation, this being more apparent for CT900.10. The pore size shrinkage is also clearly observed in clipping planes (Fig. 9C and Fig. 9D), which illustrate pore channel thickness maps before and after oxidation with exemplary regions of reduced pore size after oxidation marked by arrows.

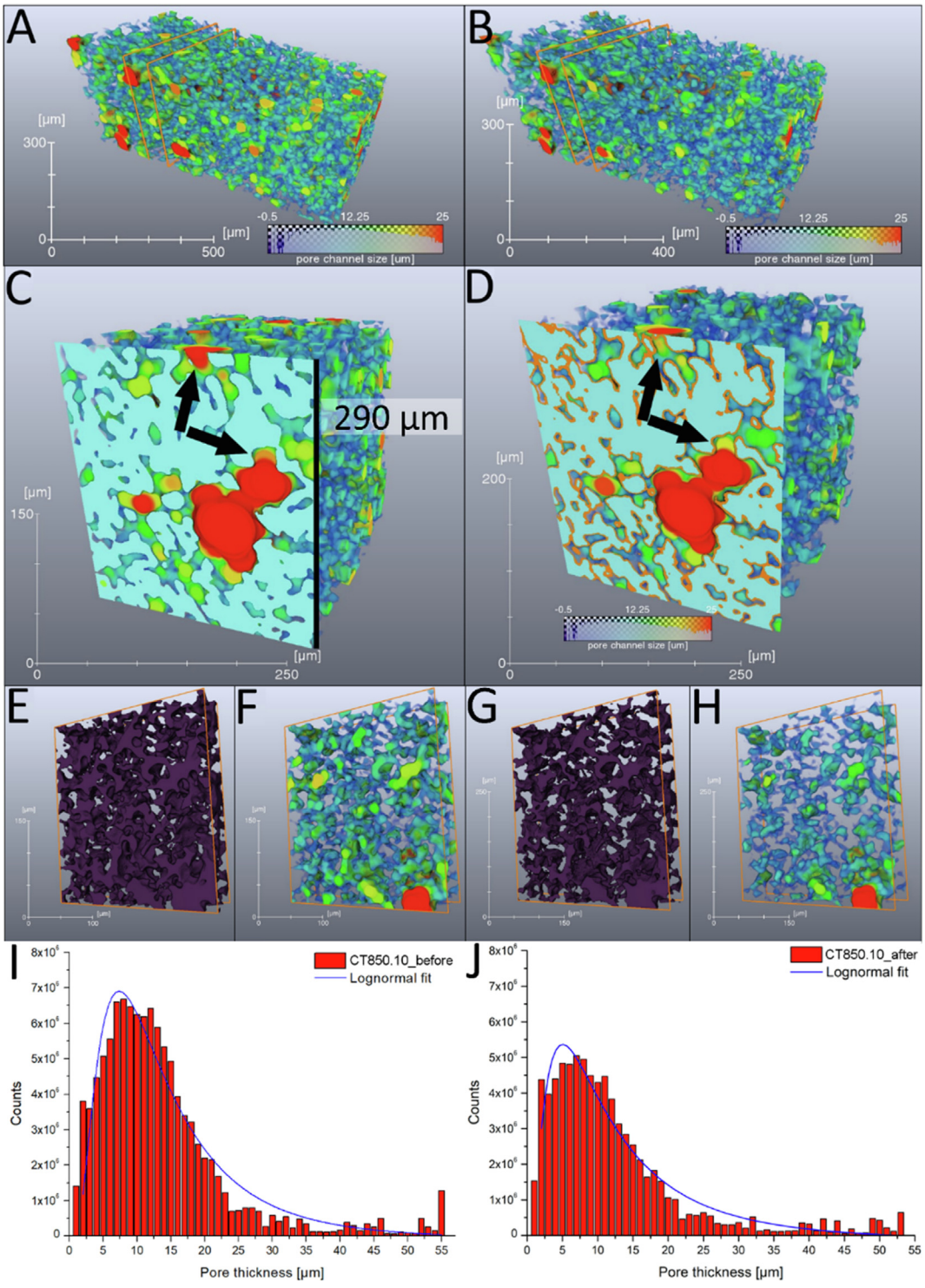

Fig. 9. A) Visualisation of pore channels thickness size for the CT850.10 sample before and B) after oxidation with exemplary clipping plane C) before and D) after oxidation. Morphology of the pore channels for the CT850.10 sample E) before and G) after oxidation with corresponding pore size distribution (F, G) and histograms of pore channels size thickness (I, J). Black arrows indicate exemplary corresponding regions of pore thickness map before (C) and after (D) oxidation.

The channel structure and changes of pore morphology before and after oxidation (purple colour), are illustrated in Fig. 9 E, G, respectively, which show volume rendering of the porosity phase obtained from material segmentation. These images show volume elements marked in Fig. 9 A and B with orange frames. The corresponding pores size distribution visualisation of the same volume fractions are presented in Fig. 9 F and Fig. 9 H. Decreasing of porosity is clearly visible not only from comparison of colour scale in the pore channels thickness 3D maps, but also from decreasing of pores volume after oxidation which is observed as reduction of purple colour phase in Fig. 9 G as compared to Fig. 9 E. In the histograms of the pore thickness maps (Fig. 9 I, J), a decrease of the average pore size is also visible, as a shift of the fitted lognormal function peak and a smaller amount of pore voxels' counts for

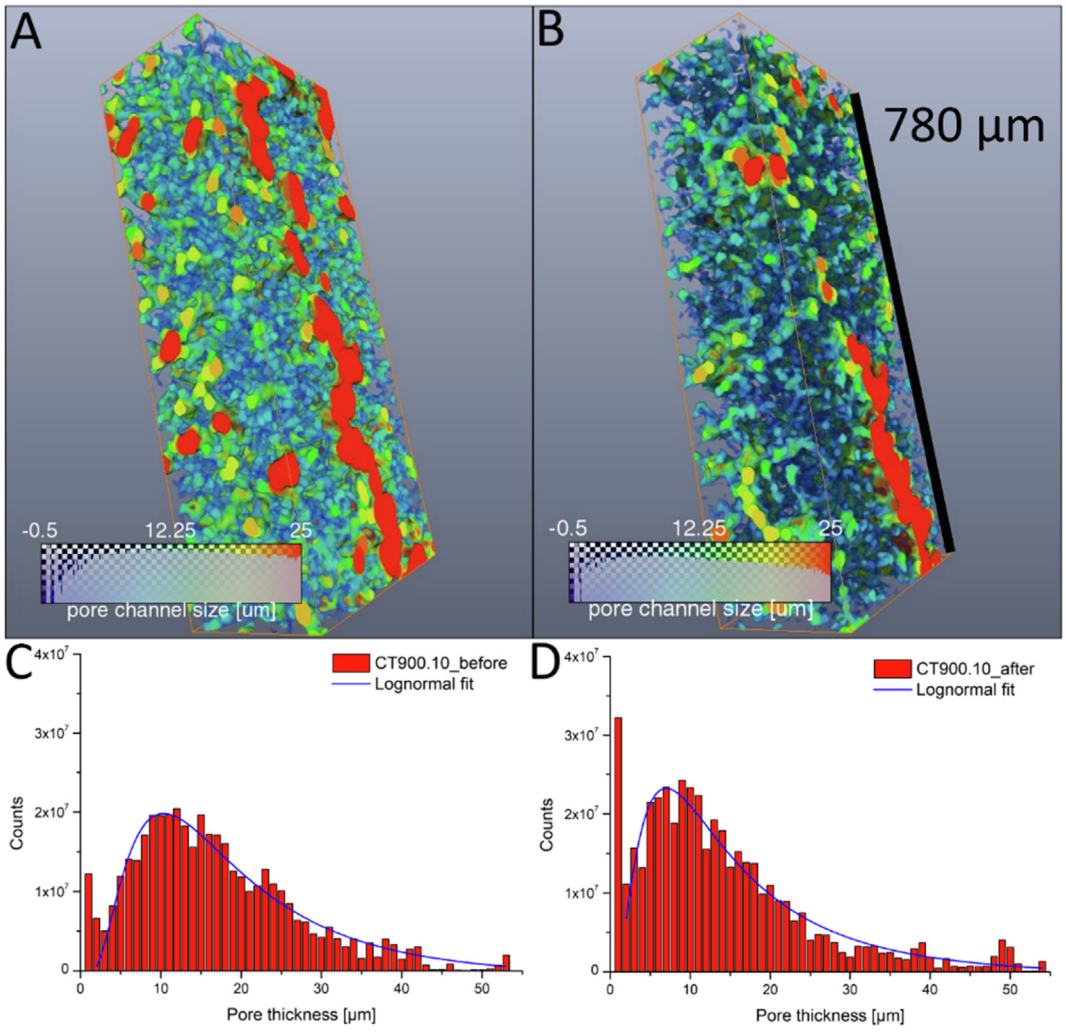

Fig. 10. Visualisation of pore channels thickness size for CT900.10 A) before B) after oxidation with C, D) corresponding histograms of pore channel size thickness.

the oxidised sample compared with the non-oxidised one. Results of evaluation of changes in pore morphology, SSA, and oxide thickness are summarized in Table 4.

4. Conclusions

A detailed study of the effect of high-temperature oxidation on the morphology changes in porous Fe22Cr stainless steel in the temperature range of 850 – 900 °C was performed using two complementary imaging techniques. Synchrotron tomographic microscopy provided insight into the complex 3-dimensional structure of various phases of the samples, while scanning electron microscopy allowed for resolving features beyond the spatial resolution of the tomographic measurements.

Tomographic microscopy was performed using a monochromatic X-ray beam, which together with the optimization of the reconstruction algorithm parameters, allowed not only for analysis of the morphology, but also for distinguishing and quantification of particular phases: the metallic core, oxide scale and porosity. Image analysis performed for the reconstructed volumes was used to analyse porosity and steel morphology changes, as well as the oxide scale growth occurring during the oxidation process. Each investigated sample was scanned before and after oxidation and in both cases, exactly the same regions were localised and analysed. Additionally, SEM images showed the microporosity and cracks of the oxide scale that were not visible in tomograms, which was essential for understanding the results of material segmentation of tomographic data.

Analysis of the oxide scale has shown that for porous alloys the 3D analysis is necessary to evaluate the thickness of the oxide scale because the measurement of oxide scale thickness performed from 2D SEM images strongly depends on the polishing plane and the angle of polishing selection. The 3D analysis proved that for longer oxidation (time effect), as well as for higher oxidation temperature (temperature effect), the oxide scale thickness increases, which is connected with the SSA growth of the alloy. After oxidation for 10 h at 900 °C (CT900.10 sample) the SSA has increased by 50 % thus, the possible oxygen-alloy contact area has also become significantly larger. However, the oxide scale is also a diffusion barrier for Cr^{3+} cations and this effect seems to counterbalance the effect of SSA growth on the oxidation process because no change of slope is observed in mass gain measurements. The increase of SSA was also confirmed by particle size analysis. For each investigated sample the average particle size decreased after oxidation which is connected with the SSA growth and similarly to this effect, the greatest fall of average particle size was observed for the most oxidised samples.

Although the SEM analysis revealed breakaway region only for the CT850.100 sample, the tomography experiment proved its occurrence also for the CT850.30 and CT900.10 samples. This

shows that the 3D analysis is necessary for oxidation research of porous ferritic alloys. Nevertheless, SEM imaging, due to its higher spatial resolution, is a complementary method that is necessary for correct interpretation and full understanding of the tomographic results. These studies show the breakaway oxidation regions after oxidation in specific conditions but the origin of these regions remains unknown. Moreover, for the CT850.30 sample a few regions of breakaway oxidation have been identified thus, the mass gain of this sample was even bigger than in the case of CT900.10 but for the sample oxidised at the same temperature for 100 h (CT850.100) only one bigger place of breakaway oxidation was detected. For establishing preferable areas for breakaway oxidation appearance and their origin, in situ tomography studies are necessary, which will be the scope of our further research.

The porosity analysis showed that it has a form of connected channels and the open porosity dominates in the investigated alloy. Although, closed porosity was also detected and its fraction has increased during the oxidation, its amount was still so low that it should have no significant effect on the alloy properties, at least in the investigated range of oxidation degree. A more important effect appeared to be the significant decrease of the size of the open pores, caused by the growth of the oxide scale in the volume of pores. For the sample with the highest degree of oxidation (for the CT850.100 sample), the average pore channel size was decreased by 24 % (taking into consideration fitted lognormal function), showing that the studied alloy cannot be efficiently used as a gas membrane at so high temperatures.

The presented study provides a new characterization method of porous ferritic alloys by quantitative analysis of distinguished oxide, alloy and pore phases. The presented tomographic analysis provided data, which can improve the understanding of porous alloys failure caused by oxidation, modelling of the porous alloys' oxidation process and allow for prediction of the porous alloy lifetime.

Declaration of Competing Interest

The authors declare that they have no known competing financial interests or personal relationships that could have appeared to influence the work reported in this paper.

Acknowledgements

This project was supported by National Science Centre Poland (NCN) Sonata Bis 8 project number 2018/30/E/ST8/00821 "High-temperature corrosion studies and development of oxidation lifetime model of alloy powders and sintered porous alloys: effects of composition and microstructure".

The authors would like to acknowledge Höganäs AB, Sweden for porous steel samples production and the Paul Scherrer Institut, Villigen, Switzerland for provision of synchrotron radiation beamtime (proposal 20181598) at the TOMCAT beamline of the Swiss Light Source.

Data availability

The raw/processed data required to reproduce these findings cannot be shared at this time as the data also forms part of an ongoing study.

Appendix A. Supplementary material

Supplementary data to this article can be found online at https://doi.org/10.1016/j.matdes.2022.110492.

References

[1] D.J. Young, High temperature oxidation and corrosion of metals, Elsevier, 2008.
[2] M.J. Pomeroy, Coatings for gas turbine materials and long term stability issues, Mater. Des. 26 (3) (2005) 223–231, https://doi.org/10.1016/j.matdes.2004.02.005.
[3] H.J.C. Voorwald, R.C. Coisse, M.O.H. Cioffi, Fatigue strength of X45CrSi93 stainless steel applied as internal combustion engine valves, Procedia Eng. 10 (2011) 1256–1261, https://doi.org/10.1016/j.proeng.2011.04.209.
[4] M. Park, J.-S. Shin, S. Lee, H.-J. Kim, H. An, H.-i. Ji, H. Kim, J.-W. Son, J.-H. Lee, B.-K. Kim, H.-W. Lee, K.J. Yoon, Thermal degradation mechanism of ferritic alloy (Crofer 22 APU), Corros. Sci. 134 (2018) 17–22, https://doi.org/10.1016/j.corsci.2018.01.022.
[5] B. Talic, S. Molin, P.V. Hendriksen, H.L. Lein, Effect of pre-oxidation on the oxidation resistance of Crofer 22 APU, Corros. Sci. 138 (2018) 189–199. https://doi.org/https://doi.org/10.1016/j.corsci.2018.04.016
[6] M. Bianco, S. Poitel, J.E. Hong, S. Yang, Z.J. Wang, M. Willinger, R. Steinberger-Wilckens, J., Van herle, Corrosion behaviour of nitrided ferritic stainless steels for use in solid oxide fuel cell devices, Corros. Sci. 165 (2020), https://doi.org/10.1016/j.corsci.2019.108414 108414.
[7] B. Öztürk, A. Topcu, S. Öztürk, Ö.N. Cora, Oxidation, electrical and mechanical properties of Crofer®22 solid oxide fuel cell metallic interconnects manufactured through powder metallurgy, Int. J. Hydrogen Energy. 43 (23) (2018) 10822–10833, https://doi.org/10.1016/j.ijhydene.2018.01.078.
[8] A. Topcu, B. Öztürk, Ö.N. Cora, Performance evaluation of machined and powder metallurgically fabricated Crofer®22 APU interconnects for SOFC applications, Int. J. Hydrogen Energy. 47 (5) (2022) 3437–3448, https://doi.org/10.1016/j.ijhydene.2021.06.036.
[9] J. Cao, M. Zheng, Z. Wang, X. Si, C. Li, X. Wang, Z. He, J. Qi, A low-temperature sealing method for metal-supported oxide fuel cell applications: Ni–Sn transient liquid phase bonding, Vacuum 187 (2021) 110048, https://doi.org/10.1016/j.vacuum.2021.110048.
[10] A. Holt, P. Kofstad, Electrical conductivity and defect structure of Cr2O3. II. Reduced temperatures (<~1000°C), Solid State Ionics 69 (1994) 137–143, https://doi.org/10.1016/0167-2738(94)90402-2.
[11] Y.H. Xiang, L.Z. Liu, J.C. Shao, H.J. Jin, A universal scaling relationship between the strength and Young's modulus of dealloyed porous Fe0.80Cr0.20, Acta Mater. 186 (2020) 105–115, https://doi.org/10.1016/j.actamat.2019.12.046.
[12] C. Witherspoon, P. Zheng, M. Chmielus, D.C. Dunand, P. Müllner, Effect of porosity on the magneto-mechanical behavior of polycrystalline magnetic shape-memory Ni-Mn-Ga foams, Acta Mater. 92 (2015) 64–71, https://doi.org/10.1016/j.actamat.2015.03.038.
[13] L. Zhao, S. Ha, K.W. Sharp, A.B. Geltmacher, R.W. Fonda, A.H. Kinsey, Y. Zhang, S.M. Ryan, D. Erdeniz, D.C. Dunand, K.J. Hemker, J.K. Guest, T.P. Weihs, Permeability measurements and modeling of topology-optimized metallic 3-D woven lattices, Acta Mater. 81 (2014) 326–336, https://doi.org/10.1016/j.actamat.2014.08.037.
[14] E. Stefan, C. Denonville, Y. Larring, M. Stange, R. Haugsrud, Oxidation study of porous metal substrates for metal supported proton ceramic electrolyzer cells, Corros. Sci. 164 (2020) 108335, https://doi.org/10.1016/j.corsci.2019.108335.
[15] M. Palcut, L. Mikkelsen, K. Neufeld, M. Chen, R. Knibbe, P.V. Hendriksen, Corrosion stability of ferritic stainless steels for solid oxide electrolyser cell interconnects, Corros. Sci. 52 (10) (2010) 3309–3320, https://doi.org/10.1016/j.corsci.2010.06.006.
[16] R. Wang, Z. Sun, J.-P. Choi, S.N. Basu, J.W. Stevenson, M.C. Tucker, Ferritic stainless steel interconnects for protonic ceramic electrochemical cell stacks: Oxidation behavior and protective coatings, Int. J. Hydrogen Energy. 44 (2019) 25297–25309, https://doi.org/10.1016/j.ijhydene.2019.08.041.
[17] A.W.B. Skilbred, R. Haugsrud, Sandvik Sanergy HT - A potential interconnect material for LaNbO 4-based proton ceramic fuel cells, J. Power Sources. 206 (2012) 70–76, https://doi.org/10.1016/j.jpowsour.2012.01.101.
[18] J.A. Glasscock, L. Mikkelsen, Å.H. Persson, G. Pećanac, J. Malzbender, P. Blennow, F. Bozza, P.V. Hendriksen, Porous Fe21Cr7Al1Mo0.5Y metal supports for oxygen transport membranes: Thermo-mechanical properties, sintering and corrosion behaviour, Solid State Ionics 242 (2013) 33–44, https://doi.org/10.1016/j.ssi.2013.04.006.
[19] D.N. Boccaccini, H.L. Frandsen, B.R. Sudireddy, P. Blennow, Å.H. Persson, K. Kwok, P., Vang Hendriksen, Creep behaviour of porous metal supports for solid oxide fuel cells, Int. J. Hydrogen Energy. 39 (2014) 21569–21580, https://doi.org/10.1016/j.ijhydene.2014.07.138.
[20] Y. Matus, L. Dejonghe, C. Jacobson, S. Visco, Metal-supported solid oxide fuel cell membranes for rapid thermal cycling, Solid State Ionics 176 (5-6) (2005) 443–449, https://doi.org/10.1016/j.ssi.2004.09.056.
[21] G. Reiss, H.L. Frandsen, W. Brandstätter, A. Weber, Numerical evaluation of micro-structural parameters of porous supports in metal-supported solid oxide fuel cells, J. Power Sources. 273 (2015) 1006–1015, https://doi.org/10.1016/j.jpowsour.2014.09.185.
[22] M. Stange, C. Denonville, Y. Larring, A. Brevet, A. Montani, O. Sicardy, J. Mougin, P.O. Larsson, Improvement of corrosion properties of porous alloy supports for solid oxide fuel cells, Int. J. Hydrogen Energy. 42 (17) (2017) 12485–12495, https://doi.org/10.1016/j.ijhydene.2017.03.170.
[23] M. Mokhtari, T. Wada, C. Le Bourlot, J. Duchet-Rumeau, H. Kato, E. Maire, N. Mary, Corrosion resistance of porous ferritic stainless steel produced by liquid metal dealloying of Incoloy 800, Corros. Sci. 166 (2020) 108468, https://doi.org/10.1016/j.corsci.2020.108468.

[24] D. Koszelow, M. Makowska, F. Marone, J. Karczewski, P. Jasiński, S. Molin, High Temperature Corrosion Evaluation and Lifetime Prediction of Porous Fe22Cr Stainless Steel in Air in Temperature Range 700–900°C, Corros. Sci. 189 (2021) 109589, https://doi.org/10.1016/j.corsci.2021.109589.
[25] P.J. Withers, C. Bouman, S. Carmignato, V. Cnudde, D. Grimaldi, C.K. Hagen, E. Maire, M. Manley, A. Du Plessis, S.R. Stock, X-ray computed tomography, Nat. Rev. Methods Prim. 1 (1) (2021), https://doi.org/10.1038/s43586-021-00015-4.
[26] K. Kapat, P.K. Srivas, A.P. Rameshbabu, P.P. Maity, S. Jana, J. Dutta, P. Majumdar, D. Chakrabarti, S. Dhara, Influence of Porosity and Pore-Size Distribution in Ti6Al4 v Foam on Physicomechanical Properties, Osteogenesis, and Quantitative Validation of Bone Ingrowth by Micro-Computed Tomography, ACS Appl. Mater. Interfaces. 9 (45) (2017) 39235–39248, https://doi.org/10.1021/acsami.7b13960.
[27] H.J. Simon, G. Cibin, C. Reinhard, Y. Liu, E. Schofield, I.C. Freestone, Influence of microstructure on the corrosion of archaeological iron observed using 3D synchrotron micro-tomography, Corros. Sci. 159 (2019) 31–34, https://doi.org/10.1016/j.corsci.2019.108132.
[28] S.S. Singh, C. Schwartzstein, J.J. Williams, X. Xiao, F. De Carlo, N. Chawla, 3D microstructural characterization and mechanical properties of constituent particles in Al 7075 alloys using X-ray synchrotron tomography and nanoindentation, J. Alloys Compd. 602 (2014) 163–174, https://doi.org/10.1016/j.jallcom.2014.03.010.
[29] J.C. Hastie, M.E. Kartal, L.N. Carter, M.M. Attallah, D.M. Mulvihill, Classifying shape of internal pores within AlSi10Mg alloy manufactured by laser powder bed fusion using 3D X-ray micro computed tomography: Influence of processing parameters and heat treatment, Mater. Charact. 163 (2020) 110225, https://doi.org/10.1016/j.matchar.2020.110225.
[30] V.D. Le, N. Saintier, F. Morel, D. Bellett, P. Osmond, Investigation of the effect of porosity on the high cycle fatigue behaviour of cast Al-Si alloy by X-ray micro-tomography, Int. J. Fatigue. 106 (2018) 24–37, https://doi.org/10.1016/j.ijfatigue.2017.09.012.
[31] M. Mokhtari, C. Le Bourlot, J. Adrien, A. Bonnin, T. Wada, J. Duchet-Rumeau, H. Kato, E. Maire, Microstructure characterization by X-ray tomography and EBSD of porous FeCr produced by liquid metal dealloying, Mater. Charact. 144 (2018) 166–172, https://doi.org/10.1016/j.matchar.2018.06.032.
[32] S. Dezecot, J.Y. Buffiere, A. Koster, V. Maurel, F. Szmytka, E. Charkaluk, N. Dahdah, A. El Bartali, N. Limodin, J.F. Witz, In situ 3D characterization of high temperature fatigue damage mechanisms in a cast aluminum alloy using synchrotron X-ray tomography, Scr. Mater. 113 (2016) 254–258, https://doi.org/10.1016/j.scriptamat.2015.11.017.
[33] A. Idhil, C.N. Borca, A.-C. Uldry, M. Victoria, M. Samaras, Investigating the structure of iron-chromium alloys using synchrotron based X-ray microanalysis, J. Nucl. Mater. 416 (1-2) (2011) 65–69, https://doi.org/10.1016/j.jnucmat.2010.11.097.
[34] Z. Wang, S. Wu, G. Kang, H. Li, Z. Wu, Y. Fu, P.J. Withers, In-situ synchrotron X-ray tomography investigation of damage mechanism of an extruded magnesium alloy in uniaxial low-cycle fatigue with ratchetting, Acta Mater. 211 (2021) 116881, https://doi.org/10.1016/j.actamat.2021.116881.
[35] A.E. Paz y Puente, D. Erdeniz, J.L. Fife, D.C. Dunand, In situ X-ray tomographic microscopy of Kirkendall pore formation and evolution during homogenization of pack-aluminized Ni-Cr wires, Acta Mater. 103 (2016) 534–546, https://doi.org/10.1016/j.actamat.2015.10.013.
[36] J. Stef, A. Poulon-Quintin, A. Redjaimia, J. Ghanbaja, O. Ferry, M. De Sousa, M. Gouné, Mechanism of porosity formation and influence on mechanical properties in selective laser melting of Ti-6Al-4V parts, Mater. Des. 156 (2018) 480–493, https://doi.org/10.1016/j.matdes.2018.06.049.
[37] N. Ali, L. Zhang, H. Zhou, A. Zhao, C. Zhang, Y. Gao, Elucidation of void defects by soft reduction in medium carbon steel via EBSD and X-ray computed tomography, Mater. Des. 209 (2021) 109978, https://doi.org/10.1016/j.matdes.2021.109978.
[38] S.K. Wilke, D.C. Dunand, Structural evolution of directionally freeze-cast iron foams during oxidation/reduction cycles, Acta Mater. 162 (2019) 90–102, https://doi.org/10.1016/j.actamat.2018.09.054.
[39] T. Um, S.K. Wilke, H. Choe, D.C. Dunand, Effects of pore morphology on the cyclical oxidation/reduction of iron foams created via camphene-based freeze casting, J. Alloys Compd. 845 (2020) 156278, https://doi.org/10.1016/j.jallcom.2020.156278.
[40] K. Kwok, D. Boccaccini, Å.H. Persson, H.L. Frandsen, Homogenization of steady-state creep of porous metals using three-dimensional microstructural reconstructions, Int. J. Solids Struct. 78–79 (2016) 38–46, https://doi.org/10.1016/j.ijsolstr.2015.09.020.
[41] K. Zhuravleva, R. Müller, L. Schultz, J. Eckert, A. Gebert, M. Bobeth, G. Cuniberti, Determination of the Young's modulus of porous ß-type Ti-40Nb by finite element analysis, Mater. Des. 64 (2014) 1–8, https://doi.org/10.1016/j.matdes.2014.07.027.
[42] B. Mortimer, P. Grieveson, K.H. Jack, Precipitation of nitrides in ferritic iron alloys containing chromium, Scand. J. Metall. 1 (1972) 203–209.
[43] G. Miyamoto, A. Yonemoto, Y. Tanaka, T. Furuhara, T. Maki, Microstructure in a plasma-nitrided Fe-18 mass% Cr alloy, Acta Mater. 54 (18) (2006) 4771–4779, https://doi.org/10.1016/j.actamat.2006.06.006.
[44] D. Paganin, S.C. Mayo, T.E. Gureyev, P.R. Miller, S.W. Wilkins, Simultaneous phase and amplitude extraction from a single defocused image of a homogeneous object, J. Microsc. 206 (1) (2002) 33–40, https://doi.org/10.1046/j.1365-2818.2002.01010.x.
[45] T. Hildebrand, P. Rüegsegger, A new method for the model-independent assessment of thickness in three-dimensional images, J. Microsc. 185 (1997) 67–75, https://doi.org/10.1046/j.1365-2818.1997.1340694.x.